# Synthesis of Micro- and Nanomaterials in CO$_2$ and CO Dielectric Barrier Discharges

Igor Belov,* Jens Vanneste, Morteza Aghaee, Sabine Paulussen, Annemie Bogaerts

Dielectric Barrier Discharges operating in CO and CO$_2$ form solid products at atmospheric pressure. The main differences between both plasmas and their deposits were analyzed, at similar energy input. GC measurements revealed a mixture of CO$_2$, CO, and O$_2$ in the CO$_2$ DBD exhaust, while no O$_2$ was found in the CO plasma. A coating of nanoparticles composed of Fe, O, and C was produced by the CO$_2$ discharge, whereas, a microscopic dendrite-like carbon structure was formed in the CO plasma. Fe$_3$O$_4$ and Fe crystalline phases were found in the CO$_2$ sample. The CO deposition was characterized as an amorphous structure, close to polymeric CO (p-CO). Interestingly, p-CO is not formed in the CO$_2$ plasma, in spite of the significant amounts of CO produced (up to 30% in the reactor exhaust).
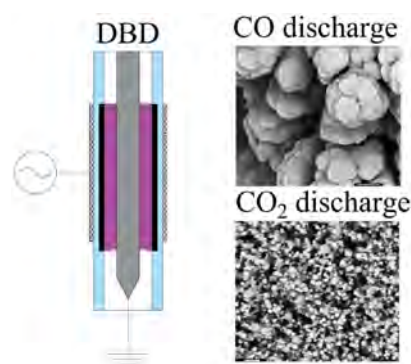
1. Introduction

The mitigation of carbon dioxide is considered as one of the grand engineering challenges of the 21st century. The transformation of CO$_2$ into a chemical feedstock or a solid product presents a promising approach toward this task, and positive economic incentives for the businesses to implement carbon dioxide capturing and treatment technologies may be created in this way. A lot of new research in the field is targeted toward the CO$_2$ solidification, and thus, the formation of added-value products, while simultaneously reducing CO$_2$ or other greenhouse gases.[1–7]

I. Belov, J. Vanneste, S. Paulussen
Sustainable Materials Management, VITO, Boeretang 200, 2400 Mol, Belgium
E-mail: igor.belov@vito.be
I. Belov, A. Bogaerts
PLASMANT, Department of Chemistry, University of Antwerp, B-2610 Wilrijk-Antwerp, Belgium
M. Aghaee
Department of Applied Physics, Eindhoven University of Technology, 5600 Eindhoven, The Netherlands

Non-thermal plasma (NTP) technology presents a versatile tool used in various industries, including environmental engineering.[8] Due to the non-equilibrium chemistry of the NTP, even thermodynamically unfavorably reactions are occurring at near-room temperature, including carbon dioxide splitting, which is a highly endothermic process, as presented in reaction 1.

$$CO_2 \rightarrow CO + 0.5O_2, \Delta H = 2.9 \, \text{eV/molecule} \qquad (1)$$
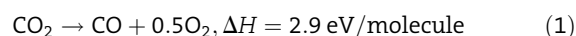
The possibility of CO$_2$ decomposition at rather low temperatures and atmospheric pressure presents an important feature of NTP systems. When combined with the utilization of renewable electric energy and the use of abundant materials for the reactor design, NTP technology is an interesting tool for the technological implementation of CO$_2$ decomposition. Several approaches toward the CO$_2$ reduction by means of NTP were explored experimentally and theoretically.[9] The dissociation of CO$_2$ or CH$_4$ in NTP reactors mainly targets the generation of gaseous products (CO, H$_2$, or a mixture of both). Nonetheless, the concept of co-generation of carbonaceous added-value solid products in discharges of greenhouse gases was also explored for thermal

plasmas[10–17] as well as NTP setups.[18–22] In the majority of these studies the deposition of carbon was associated with the decomposition of the initially present or formed methane (or higher hydrocarbons) according to the endothermic reaction (reaction 2)[23]:

$$C_nH_m \rightarrow nC_s + \frac{m}{2}H_2 \qquad (2)$$

Carbon reduction in pure CO_2 plasmas presents a more challenging task due to the high dissociation energy of CO (11 eV vs. ∼5 eV for CH_x).[24] However, the disproportionation reaction (Reaction 3) is known to be a more effective path for CO decomposition (activation energy $E_a \sim 5.5$ eV/molecule), and this reaction can also be stimulated by plasma exposure due to vibrational and electronic excitation.[8]

$$CO + CO \rightarrow C + CO_2, \Delta H = 5.5 \text{ eV/molecule},$$
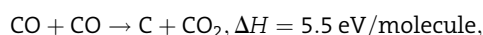
$$E_a = 6 \text{ eV/molecule} \qquad (3)$$

In this paper, we study the formation of carbonaceous solid products in pure CO_2 and CO Dielectric Barrier Discharge (DBD) systems, which represent a popular NTP approach for carbon dioxide decomposition.[25–40] Interestingly, coke deposition is mostly not observed in such DBD reactors when working with CO_2. [25–27,35–40] On the other hand, Li et al. reported the implementation of a high-permittivity dielectric material ($\varepsilon > 200$) in a DBD reactor, which resulted in an enhanced conversion rate, high-amplitude discharge currents, and the formation of presumably carbonaceous deposits.[32] Furthermore, Tomai et al. utilized a DBD cell operating with super-critical CO_2 to synthesize nanostructured carbon materials.[41,42] Mori et al. generated carbon nanotubes and other nanomaterials in a hybrid DBD-Solid Oxide Electrolyser Cell (DBD-SOEC) reactor.[22] When oxygen was in situ extracted from the discharge zone, the CO_2 conversion rate was reaching 100%.

In packed-bed DBD reactors (i.e., DBD systems in which the discharge space is filled with dielectric beads[40,43] solid products of the CO_2 discharge were observed and associated with the electric field enhancement near the contact points of the dielectric beads.[44] In the recent work of Yap et al., it was demonstrated that a highly reactive CO_2 plasma can not only form carbonaceous structures, but also etch the material of the glass beads and re-deposit composite structures.[45]

In contrast to CO_2, a rather effective deposition process can be realized in a carbon monoxide atmosphere via chemical vapor deposition systems[46–49] as well as plasma setups.[50–52] Furthermore, Mori et al. demonstrated the production of various nanomaterials via vacuum DC[53,54] and microwave (MW)[55–58] discharges operating in carbon monoxide atmosphere with Ar, H_2, and O_2 admixtures. However, rather limited information is available on atmospheric pressure CO discharges. Zheng et al. found solid carbonates when using CO as a feed gas in a DBD reactor instead of CO_2.[29] Geiger and Staack presented a study of a CO DBD and characterized the formed deposits as carbon suboxide (C_3O_2) polymer.[59] Unfortunately, the morphology and crystallinity of the achieved solid products were not discussed in both cases.

In our previous work,[60] the deposition of a slightly conductive coating on the reactor walls was observed in CO_2 discharges. This phenomenon was associated with the high energy input regime (up to 80 eV/molecule), yielding a large CO_2 dissociation rate (20–50%), and thus, high CO concentrations (10–30 mol.%). It was believed that the disproportionation reaction (reaction 3) was responsible for film deposition. As already noted, observations of deposits formation in pure CO_2 discharges are quite rare, and only a few studies on atmospheric pressure CO plasmas are available. For this reason a comprehensive analysis and comparison of CO and CO_2 discharges, and their solid products is very interesting from both a material science and a plasma chemistry point of view.

In this work, CO_2 and CO discharges as well as their solid products were compared in a cylindrical DBD reactor. In this way our initial hypothesis of CO formation and disproportionation in CO_2 plasma can be verified. Hence, the question to be answered is the following: will the CO and CO_2 discharges give rise to similar deposits at similar conditions and if not, what are the main differences between those plasmas?

2. Experimental Section

2.1. Reactor Set-Up

The experimental setup is schematically shown in Figure 1. A discharge gap of 0.5 mm is obtained between two concentric cylinders, that is, a grounded stainless steel central electrode (outer diameter 25 mm) and a dielectric tube (26 mm inner diameter, 29 mm outer diameter) made of borosilicate glass. It was demonstrated by Aerts et al. that using a smaller gap allows the rise of the reactor capacitance and a decrease of the onset voltage due to enhanced electric field intensity, which is beneficial for the system performance.[36] A stainless steel mesh is wrapped at the outside of the dielectric tube, acting as an outer electrode and at the same time defining the length of the plasma discharge (215 mm). The outer electrode arrangement is cooled with deionized water with a controlled conductivity of less than 0.5 μS · m. In this way, local overheating of the reactor and parasitic discharges on the sharp edges of the mesh are prevented. The central electrode is cooled with drinking water of standard quality.

The inner electrode is grounded while the outer electrode is connected to a power supply with a maximum peak-to-peak voltage of 40 kV, and a variable frequency between 2 and 90 kHz (AFS G10S-V generator, AFS GT-10…80 transformers). The applied voltage and the total current are measured by a high voltage probe
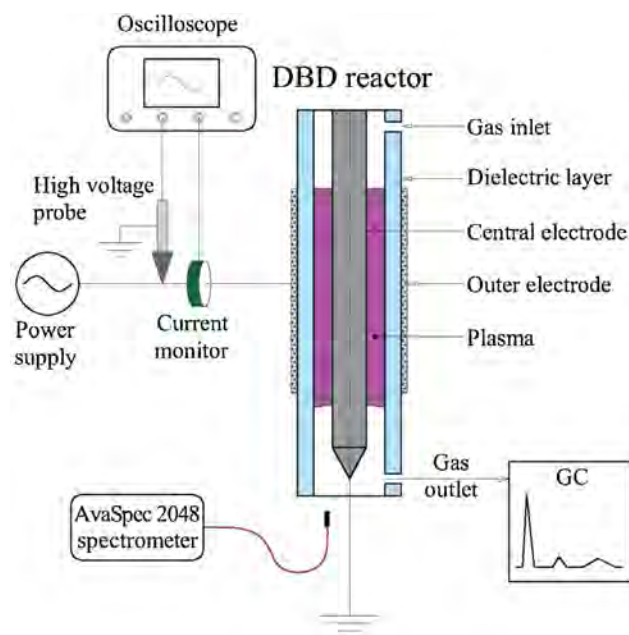
Figure 1. Experimental setup of the tubular dielectric barrier discharge reactor in the Metal-Dielectric (MD) configuration.

(Tektronics P6015A) and a Rogowski-type current meter (Pearson Model 4100, 35 MHz), respectively.

The process is monitored by a 25 MHz PicoScope 2205 digital oscilloscope. Due to the design of the reactor it was not possible to introduce an external measuring capacitor in the electrical circuit of the reactor. The energy input in the discharge is controlled by setting the power of the generator and calculating the corresponding value (Equation 4):

$$P_{\text{Input}} = \frac{1}{T} \int_0^T I(t)U(t)dt \qquad (4)$$

where T is the period of the AC, and $I(t)$ and $U(t)$ are the measured current, and applied voltage signals, respectively.

The specific energy input (SEI) is used to compare the conversion efficiencies of the various set-ups (Equation 5)[61]:

$$\text{SEI(eV/molec.)} = \frac{P_{\text{Input}}(W) \cdot 60(\text{s/min})}{\text{Flow rate (mLmin}^{-1}) \cdot 3 \cdot 92(\text{J} \cdot \text{molec} \cdot /\text{eV} \cdot \text{mL})} \qquad (5)$$

The value 3.92 stems from the conversion of units, as described in detail in the reference.[61]

2.2. Process Conditions

The discharge gap of 0.5 mm and the 215 mm steel mesh length yield a total volume of the plasma zone equal to 8.6 mL. The gas flow rate is varied from 0.05 Standard Litre per Minute (SLM) to 1.2 SLM, yielding a residence time in the plasma between 10.3 and 0.43 s. Gases of premium quality (99.95% purity, Air Products) are used in these experiments. The gaseous products of the reaction are

analyzed by gas chromatography (Trace-GC, Interscience), equipped with a Thermal Conductivity (TCD), and Flame Ionization (FID) detector. The ozone production was not monitored during the discharge.

A survey fiber spectrometer (Avantes, AvaSpec 2048, 180–750 nm range) with 2.3 nm FWHM resolution is used for monitoring the process, collecting light through a 6 mm collimating lens. The lens was pointed on the discharge gap through an optical window (90% transmittance in the 320–600 nm range) installed downstream the reactor parallel to the electrode axis.

2.3. Material Preparation and Characterization

The material was collected from the inner surface of the dielectric tube in the form of a powder. Typically the amount of the collected sample was in the order of 0.035–0.5 g after 1–5 h of discharge operation.

A field emission gun scanning electron microscope (FEGSEM, JSM-6340F, JEOL) was used to obtain images to evaluate the microscopic structure and to determine the elemental composition of the formed structures.

Fourier Transform Infrared spectroscopy (FTIR) was performed with a Thermo Nicolet Nexus spectrometer in Attenuated Total Reflectance (ATR) mode. Typically 0.015 g of powder was spread over the diamond crystal and pressed to improve the contact between the crystal, and the sample. The spectrum was recorded between 4000 and 400 cm^{-1} over 128 scans in order to achieve an acceptable signal to noise ratio.

X-Ray Diffraction (XRD) patterns were recorded using PHILIPS X'PERT PRO with Cu Kα radiation in a 2θ range between 0° and 120° (0.04° scan step size) at room temperature.

Raman measurements were employed to identify the chemical bonding characteristics of carbon with a Renishaw Raman Microscope with a 1800 lines mm^{-1} grating and using a laser line of 512 nm as the excitation source.

Finally, an X-ray Photoelectron Spectroscopy (XPS) system PHI-5600ci (Physical Electronic) was used to perform quantitative elemental analysis at the surface of the solid materials by spectroscopy of the emitted photo electrons. The powder was applied on indium foil and measured from the area with a diameter of Ø800 μm.

3. Results

3.1. Discharge Comparison

3.1.1. Electrical Signals

The plasma obtained in the DBD is composed of numerous microdischarges (also called filaments) with a typical channel diameter of 0.01–1 mm.[62] Each filament might be considered as a single chemical reactor, where reactions are driven by the charged particles accelerated in the electric field.[63] The charge transfer of a microdischarge

(MD) is limited by a dielectric layer, preventing spark, or arc (i.e., constricted high-current, thermal discharges) formation. In this way, the low-current filaments are spread over the barrier surface, maintaining rather low-temperature non-equilibrium conditions in the whole reactor volume. Interestingly, in DBD systems one cannot directly control the discharge current by increasing the applied voltage: the value is determined mainly by the gas composition, gap size, and the dielectric material. Moreover, a higher input power (or applied voltage) will not result in an enhancement of the charge transfer through a single filament, but it will rather increase the number of MDs per HC.[8,39]

The electrical signals of the CO_2 and CO discharges obtained at the same power are compared in Figure 2. The CO_2 plasma gives rise to an asymmetric current waveform with respect to the positive and negative half-cycles (HC) of the applied voltage. High-amplitude (up to 0.5–1 A) sparse current pulses and simultaneous voltage drops (up to 0.5–1 kV) were observed during the positive HC. A more stable filamentary regime with smaller current peaks of about 50 mA (barely visible in Figure 2[a] due to the scale) and no distortion of the applied voltage can be noted in the negative HC. The asymmetry of the CO_2 DBD current waveform is discussed in our previous work.[60] This behavior was found to be consistent for O_2 and CO_2 gases and was changing with the appearance of a coating inside the dielectric tube. It can be attributed to the electronegativity of the CO_2 molecule and the formation of O_2 in the CO_2 discharge.

On the other hand, the discharge current in the CO plasma (cf. Figure 2[b]) is symmetrical, with 35–50 mA amplitude current bursts measured in both HCs (also barely visible in Figure 2[b]).

In our system, it is not possible to retrieve precise information regarding a single MD due to the ignition of several filaments at the same time, and thus, overlapping signals in the current waveform. However, we can conclude that intensive and sparse filaments can be observed in the CO_2 discharge (at least in the positive HC) while more uniformly spread lower energy (i.e., lower current) MDs are present in the CO DBD.

3.1.2. Gas Phase Analysis

The efficiency of the CO_2 dissociation and the exhaust composition of the CO_2 discharge were evaluated by means of gas chromatography, which allows separation and quantification of the compounds present in the gas mixture due to differences in column retention times. The concentrations of the products in the exhaust of the DBD reactor are calculated according to Equation 6:

$$\text{Molar concentration}(CO_2/CO/O_2)(\%)$$

$$= \frac{[CO_2/CO/O_2]}{[CO_2 + CO + O_2]} \times 100\% \qquad (6)$$

The results of the CO_2 dissociation experiments in the DBD reactor are presented in Figure 3. By varying the specific energy input (SEI) in the range between 5 and 115 eV/molecule, conversion levels between 20 and 50% were obtained. Interestingly, by increasing the SEI above 60 eV/molecule, a plateau was reached with respect to the dissociation degree. The ratio of the product yields ([CO]/[O_2] $\sim$ 2.1) was close to the stoichiometric one, indicating the dominance of the overall Reaction 1. The data presented in Figure 3 are based on the variation of both flow and power, as the specific energy input is known to be the prevailing parameter in the CO_2 dissociation process.[36]
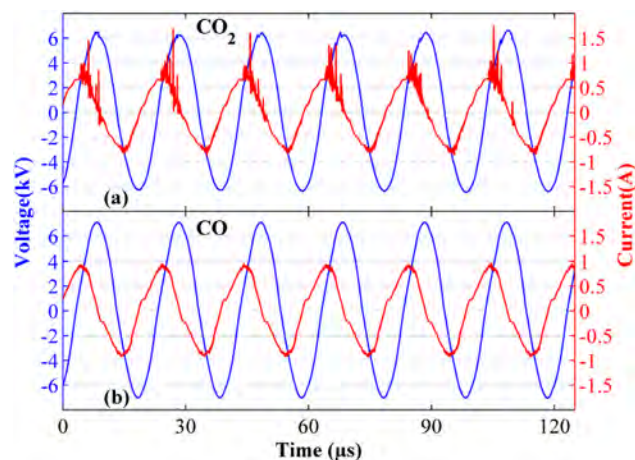

Figure 2. Electrical signal of the (a) CO_2 and (b) CO DBD; (Discharge power: 600 W; gas flow rate: 1 SLM; frequency: 50 kHz.).
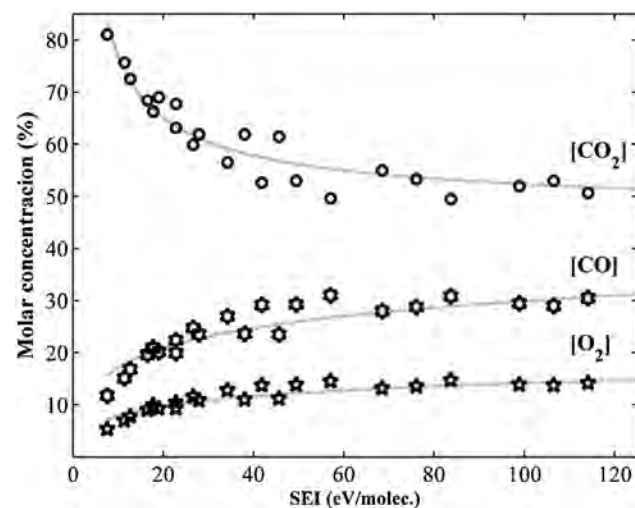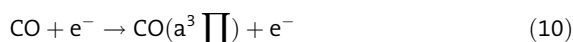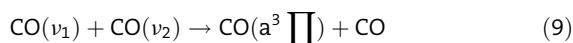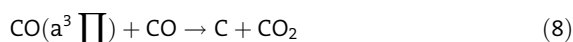

Figure 3. Molar concentrations of the CO_2 discharge products as a function of the specific energy input (SEI).

In the case of the CO discharge, only CO and low amounts of CO_2 (order of 1–6 mol.%; cf Table 1) were found in the outlet gas of the reactor. The amount of CO_2 produced was proportional to the specific energy input (cf. Table 1). Interestingly, no O_2 could be detected in the reactor exhaust by means of gas chromatography.

As already noted, a higher power input increases the number of MDs per half-cycle, thus, a single molecule will more often be subject to electron impact collisions, resulting in higher CO_2 conversion rates.[39] According to Aerts et al., electron impact excitation followed by dissociation (cf. Reaction 7) is dominant for a DBD plasma and is the major reaction in the CO_2 decomposition process.[64]

$$CO_2 + e^- \rightarrow CO_2{}^* + e^- \rightarrow CO + O + e^- \tag{7}$$
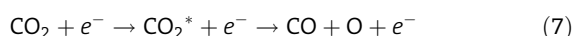
For the non-equilibrium CO plasma, it was demonstrated that the excited molecule $CO(a^3\prod)$ participates in Reaction 8 and it can be produced by vibrational, and electronic excitation (cf. Reactions 9 and 10, respectively).[65] This might be the mechanism of CO_2 production in a CO discharge. Thus, the higher CO_2 formation upon increasing SEI (cf. Table 1) can be purely explained by the higher residence time.

$$CO(a^3\prod) + CO \rightarrow C + CO_2 \tag{8}$$

$$CO(\nu_1) + CO(\nu_2) \rightarrow CO(a^3\prod) + CO \tag{9}$$

$$CO + e^- \rightarrow CO(a^3\prod) + e^- \tag{10}$$

It is important to mention that gas chromatography allows only the evaluation of the overall reaction products, while within the discharge, a more complex mixture of species contributes to the reactions taking place. For instance, it is known that also atomic oxygen and ozone are formed in the CO_2 plasma,[36] but special techniques are needed to detect and quantify them.[37,66,67]

3.1.3. Optical Emission Spectroscopy

Optical emission spectroscopy is a popular technique for non-invasive in situ plasma diagnostics. One can obtain valuable information on excited atomic and molecular states, and determine the rotational, vibrational, and electronic excitation temperatures of the plasma.[68]

The spectrum of the filamentary CO_2 plasma (cf. Figure 4 [a]) consists of the Fox system $CO_2/CO_2{}^+$ lines in the range of 300–420 nm, the CO 3rd positive band (CO(3P) at 280–360 nm), CO Angstrom bands (CO[A]) in the range between 450 and 700 nm, and a continuum part with a maximum at about 450 nm.[69–72] No distinct C_2 lines were observed during the CO_2 experiments even at the highest energy input regimes. Interestingly, atomic Fe lines (320–440 nm) were observed in the first 1–2 h of the DBD reactor operation. The Fe peaks are hard to spot in a CO_2 discharge due to overlap with the CO_2/CO lines in the same wavelength region. To better illustrate this effect, the spectrum of an O_2 discharge is shown in Figure 4(c). The spectrum consists mostly of a continuum part, and thus, the iron lines are much more clearly visible. In this case, it was also found that the iron lines were the brightest at the initiation of the discharge ("Initial spectrum" in Figure 4[c]) and they also disappeared after 1–2 h of operation ("Stable regime"). A similar behavior was thus, found for the CO_2 discharge as well. The Fe species detected by OES obviously originate from the central stainless steel electrode, which is covered with a smooth black coating after discharge operation.

Table 1. CO_2 production in the CO discharge at 400 W and various feed flow rates (0.05–1 SLM), and corresponding specific energy input (SEI) values and gas residence time.

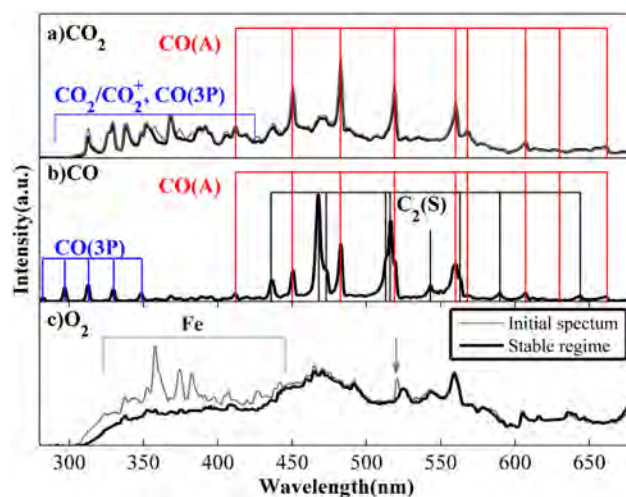| 400 W CO discharge			
[CO_2] [mol.%]	Feed flow rate [SLM CO]	SEI [eV/molec.]	Res. time [s]
0.8	1	6.1	0.5
1.6	0.5	12.1	1.03
2.5	0.25	24.3	2.07
6.2	0.05	121.7	10.2

Figure 4. Measured optical signals of a DBD plasma in (a) CO_2; (b) CO; and (c) O_2, at 600 W and 1 SLM gas flow rate.

The emission spectrum of the CO DBD is presented in Figure 4(b). Similar to the results reported by Geiger, it consists of the CO 3rd positive (CO(3P); 280–360 nm), CO Angstrom (CO[A]; 450–700 nm) and C_2 Swan bands (C_2[S]; 430–660 nm).[59] Moreover, the intensity of the C_2(S) lines increases upon increasing CO flow rate at constant input power, as demonstrated in Figure 5. The spectra presented in this picture are given in normalized units, relative to the 482.8 nm line (the brightest CO[A] line). It can be seen that the relative intensity of the C_2 peaks rise drastically with increasing CO feed flow rate.

The absence of C_2 lines in the CO_2 discharge spectra is quite typical for non-thermal plasma systems.[37,41] The Swan band is however, observed in atmospheric CO_2 MW discharges.[73–75] On the other hand, Kameshima et al. reported the emission of C_2 lines in a CO_2 DBD system, and correlated this to the removal of carbon deposits of the preceding CO_2—CH_4 discharge.[76] Tomai et al. also observed Swan bands in a CO_2 DBD when increasing the pressure above atmospheric pressure up to 2 MPa.[41] CO non-equilibrium plasmas, in contrast, do often contain C_2 bands in their emission spectra.[53,54,56,59,77] Interestingly, an admixture of oxygen or hydrogen can cause the suppression of these lines and subsequently also of the carbon deposition, as noted by Mori.[54] One might argue that the oxygen-rich atmosphere in the CO_2 plasma is responsible for the depletion of C and C_2O via the Reactions 11–13.

$$O + C_2O \rightarrow 2CO \tag{11}$$

$$O_2 + C \rightarrow CO + O \tag{12}$$

$$CO_2 + C \rightarrow 2CO \tag{13}$$

As C and C_2O are the precursors of the C_2-radical (cf. Reactions 14–16 below), this might explain the suppression of the Swan bands in the atmospheric pressure CO_2 DBD.

The appearance of atomic iron lines in the CO_2 discharge spectrum might be associated with intensive oxidation and ablation of the stainless steel electrode surface. A somewhat similar behavior of metal atomic lines was found for aluminum foils exposed to low-pressure oxygen plasmas.[78,79] The extinction of the bands with increasing exposure time can be explained by the formation of a barrier oxide layer on the treated surface and the subsequent suppression of material diffusion to the gas phase.

The higher C_2 Swan relative line intensities for higher CO flow rates shown in Figure 4(b) are at first glance somewhat contradictory to the data presented in Table 1. Indeed, in our study, we associate the formation of C radicals and CO_2 in a
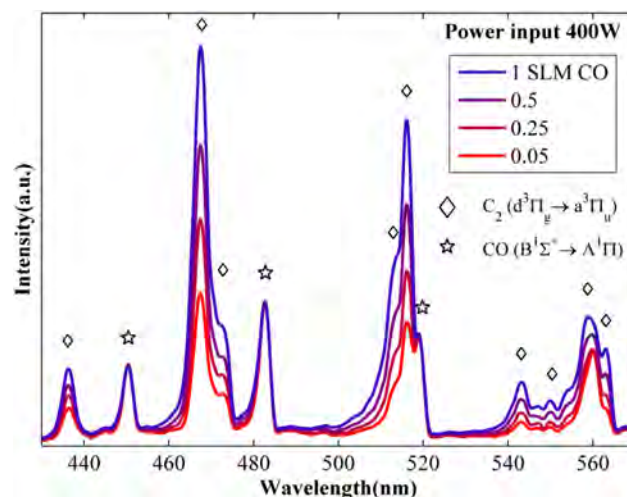

Figure 5. Emission spectrum of the CO discharge at 400 W and various feed flow rates (normalized at 482.8 nm).

CO plasma with the disproportionation reaction (Reaction 3 presented in the Introduction). Thus, one might expect that a higher CO_2 production would indicate that similarly more C, and thus, also more C_2 species are formed, making the C_2(S) bands more prominent. However, the CO_2 concentration grows upon decreasing CO flow rate, while the C_2(S) intensity shows the opposite trend. However, according to Caubet, the C_2-radical creation is governed by Reactions 14–16 and is shown to be stimulated by a higher CO concentration.[77] This behavior might be applicable to our system as well and explain the enhancement of the C_2(S) lines upon increasing CO feed flow rate.

$$C + C + M \rightarrow C_2 + M \tag{14}$$

$$C + CO \rightarrow C_2O \tag{15}$$

$$C + C_2O \rightarrow C_2 + CO \tag{16}$$

3.2. Solid Products Analysis

In this section the properties of the micro- and nano-structures formed in the CO and CO_2 discharges will be analyzed. The comparison of the CO and CO_2 DBD deposits was made for a power of 600 W and 1 SLM gas flow rate (corresponding to a SEI ~ 9 eV/molecule). It is important to mention that the synthesis process was not optimized in any way, although the energy input regime was empirically chosen in order to maximize the growth rate of solid products in the CO_2 discharge.

Deposits were collected in the form of a powder from the inner surface of the dielectric tube (cf. Figure 6). The 600 W

discharge with 1 SLM gas flow generated 15 mg min^{-1} of solid products for the CO feed (denoted as "COd") and 0.15 mg min^{-1} for the CO_2 DBD ("CO2d"). These numbers are approximations due to the non-optimized collection system and are estimated upon the weight of the gathered material. For the same reason, a deeper investigation of the relation between growth rate and energy or power input is beyond the scope of this paper.

The deposition of the CO2d sample can be monitored via the increase of the current peaks intensities during the negative HC of the applied voltage, a property described in our previous work.[60] The coating of the inner surface of the glass tube and the corresponding distortion of the current waveform can be clearly observed after 1 h of discharge operation at the given conditions. However, the CO2d sample (45 mg) was collected after 5 h of CO_2 discharge operation. An amount more than sufficient for analysis of the COd powder (>300 mg) was collected already after 30 min of the discharge operation. The CO DBD was tested to operate stably after 1 h of work without discharge extinction.
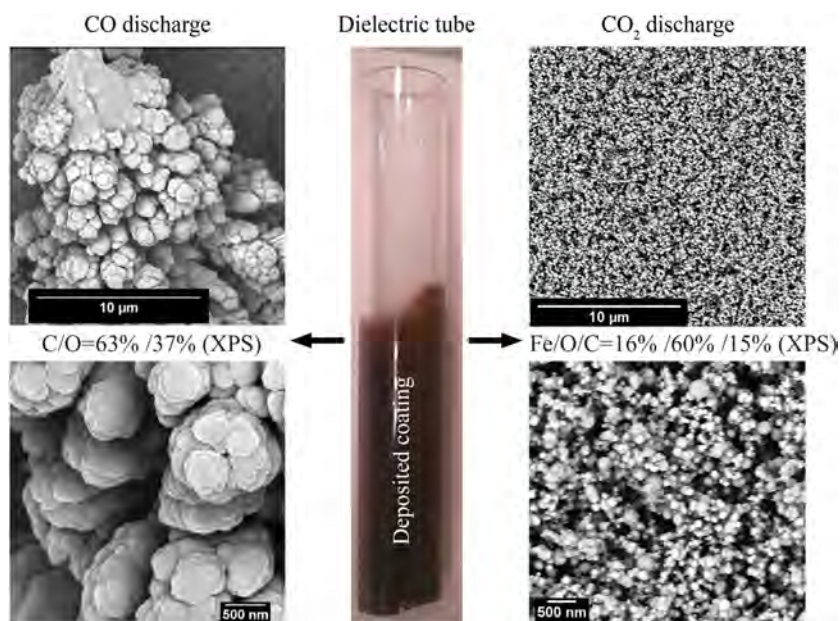
3.2.1. Morphology and Elemental Composition

The SEM images of the formed structures are presented in Figure 6. XPS analysis is employed to verify the elemental composition of the deposits. Pointy micrometer-scale structures are formed in the CO plasma. Somewhat similar morphology of carbon structures was attributed as a "dendrite" in the literature.[80,81] An atomic concentrations C/O = 73%/27% were obtained by EDS, while the

C/O = 63%/37% concentrations were measured by XPS. Variations in energy input resulted in slight morphological variations, as depicted in the SEM image of the 400 W − 0.25 SLM CO discharge deposits (cf. Figure 7). A somewhat more disordered or irregular structure could be observed when compared to the deposits obtained in the CO discharge at the higher flow rate of 1 SLM; Figure 6, left). However, the appearance of the deposited material, the pointy dendrite-like structure, is preserved.

The CO_2 discharge deposits a coating composed of spherical nanoparticles, 10–300 nm in diameter (see Figure 6, right). A substantial degree of particle agglomeration can be observed on the STEM image in Figure 8. EDS analysis revealed the presence of iron, oxygen, carbon with atomic concentrations of Fe/O/C = 13%/50%/30%, and traces of the stainless steel alloying elements (Cr, Mo, Ni, Si) with overall atomic concertation of 7%. Interestingly, the XPS measurements showed a somewhat different composition, that is, Fe/O/C = 16%/60%/15% with 9% concentration of trace elements. This can be explained by difference in the probing depth of the two techniques.

3.2.2. Structural Characterization

Thorough characterization is a necessary step for identification of the material properties and at the same time it provides information regarding the possible synthesis mechanisms of the solid products. FTIR, Raman Spectroscopy, and XRD analysis were applied to characterize the achieved structures.

CO discharge   Dielectric tube CO_2 discharge

C/O=63% /37% (XPS) ← Deposited coating → Fe/O/C=16% /60% /15% (XPS)

Figure 6. SEM images of the CO and CO_2 discharge products (denoted as COd and CO2d) at 600 W and 1 SLM (9.1 eV/molecule).
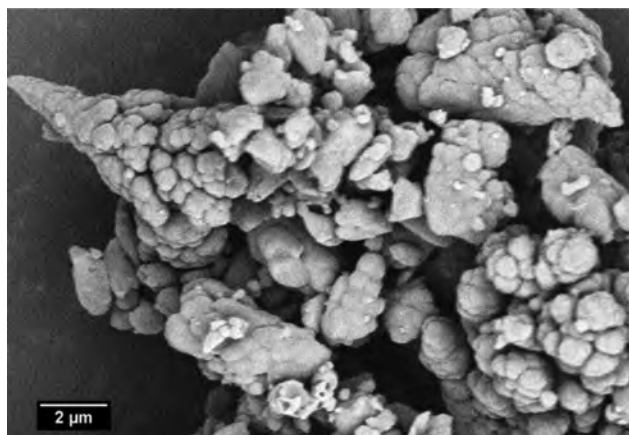
Figure 7. SEM image of the CO discharge product (COd) at 400 W and 0.25 SLM (24.3 eV/molecule).

3.2.2.1. FTIR

FTIR diagnostics allows determining the nature of the chemical bonds present in the studied material. The transmittance spectrum of the COd sample (cf. Figure 9) shows prominent carbon-oxygen (1720 and 1220 cm^{-1} for the double and single bonds, respectively) and carbon-carbon (1625 cm^{-1}) peaks. The 1400 cm^{-1} peak might be attributed to ether structures.

The variation of the CO gas flow rate (and thus SEI) results in shifts of the C=O and C—O peaks, as illustrated in Figure 10. For instance, the C=O peak at 0.05 SLM is located at 1720 cm^{-1}, while at 1 SLM it appears as a double peak at 1785 and 1730 cm^{-1}.

The Fe—O (580 cm^{-1}) peak dominates the FTIR spectrum of the CO2d sample (cf. Figure 9).[82] In addition, smaller peaks at 1630 cm^{-1}, and a broad one at 1350 cm^{-1} can be attributed to C=C and C—O bonds, respectively.

The presence of various carbon-oxide and carbon-carbon bonds can be related to the random polymeric network generated in the CO discharge. The product of the plasma[59] and pressure-induced[83] solidification of CO is referred as polymerized CO (p-CO). In these papers p-CO is compared to a carbon suboxide polymer (C_3O_2) via observing one or more of the fundamental C_3O_2 absorption peaks (near 1511, 1365, 806 cm^{-1}) in the FTIR spectra. In the same way, we can highlight the 1535 and 811 cm^{-1} peaks in Figure 10, indicating the similarity of COd to a C_3O_2 polymer.

A similar shift of the C=O peak as illustrated in Figure 10 upon different gas flow rates was also observed for pressure-induced p-CO, when the solid deposits were exposed to a 100 °C atmosphere.[84] The peak shift was attributed to degradation of the polymer structure and increased disorder. Moreover, a further temperature increase up to 200 °C resulted in disappearance of the
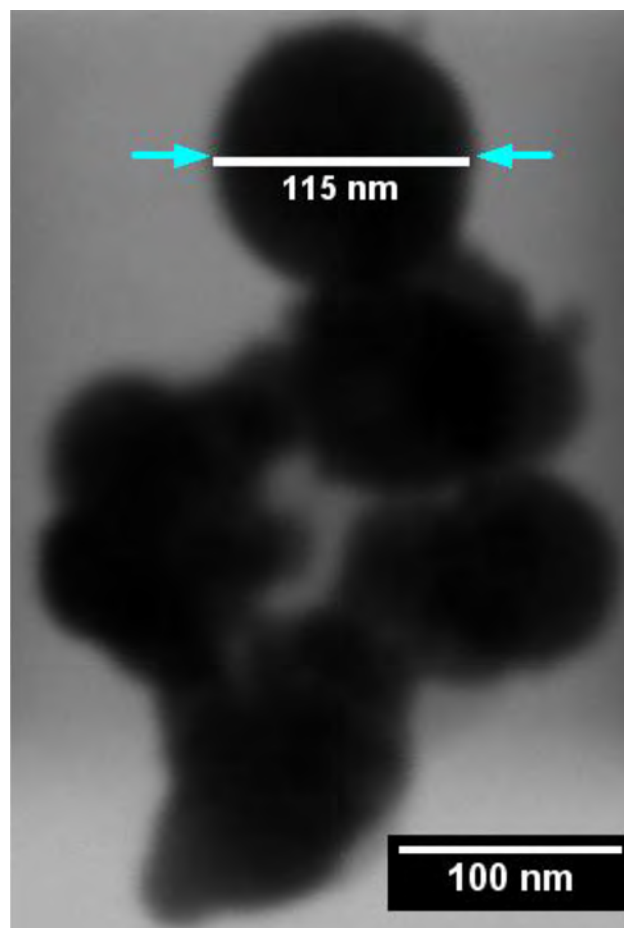

Figure 8. STEM image of nanoparticles agglomerate formed in the CO_2 discharge at 600 W and 1 SLM (9.1 eV/molecule).

C=O peak, which was explained by a loss of oxygen and the formation of a purely graphitic structure. In our study, a variation of the SEI in the range between 6 and 120 eV/molecule did not drastically change the FTIR spectrum of the COd sample even at the highest energy input used, except for the small shifts illustrated in Figure 10. This suggests that our experiments did not yield a significant degradation of the polymer structure upon increasing SEI. Moreover, very similar spectra are found in the work of Lipp et al. and Geiger et al.[59,83] Interestingly, the CO polymer structure presented by Lipp was prepared by pressure-induced polymerization, while Geiger utilized a DBD plasma system with a SEI of 0.1–l.5 eV/molecule.

We can conclude that in the broad SEI range investigated, the CO discharge yields the deposition of a polymer-like (p-CO) structure, composed of C=O, C=C, and C—O groups. For the CO2d sample, on the other hand, FTIR does not provide much information due to largely inorganic structure.
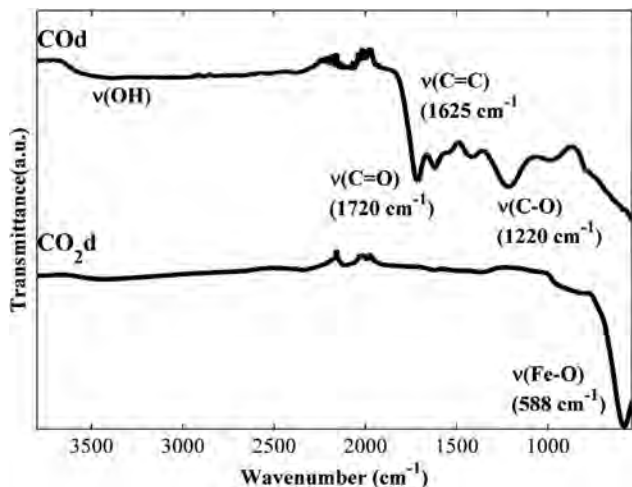
Figure 9. FTIR spectra of the COd and CO2d samples, formed at 600 W and 1 SLM (9.1 eV/molecule).
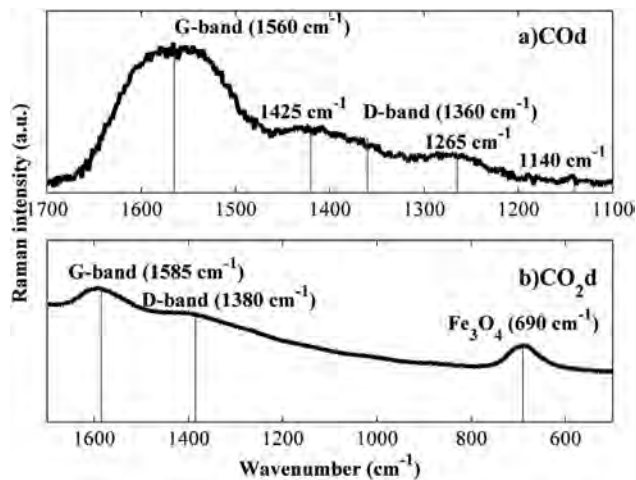

Figure 11. Raman spectra of the COd and CO$_2$d samples, formed at 600 W and 1 SLM (9.1 eV/molecule).

3.2.2.2. Raman Spectroscopy

Raman spectroscopy was used to differentiate between different phases of the deposited materials. The Raman spectrum of the COd sample (cf. Figure 11[a]) contains a pronounced G-band (1560 cm^{-1}) which is characteristic for graphitic carbon structures.[85] The D-band (1360 cm^{-1}) corresponds to disordered structures and is not so intensive ($I_D/I_G \sim 0.3$), while largely overlapping with the 1425 cm^{-1} peak, which has a somewhat contradictory interpretation in literature.[86]

The presence of the similar G and D-bands in the spectrum of the CO2d sample (cf. Figure 11[b]) confirms the presence of the C=C and C—O carbon bonds, which were only partially visible in the FTIR spectrum. The large peak at 690 cm^{-1} can be attributed to the Fe$_3$O$_4$ structure.[87]

3.2.2.3. XRD

By means of XRD the inner surface of solid materials can be probed and a distinction can be made between amorphous, and crystalline phases. The assumption that the COd sample would be amorphous is supported by Figure 12. However, small peaks that can be attributed to graphitic planes (001) and (002) are spotted around 19° and 28°, respectively.

The XRD spectrum of the CO2d is composed of multiple magnetite (Fe$_3$O$_4$ iron oxide) peaks, while smaller Fe lines can be found as well. The measurements confirm the assignment of Fe—O and Fe$_3$O$_4$ peaks, which were observed in the FTIR and Raman spectra, respectively.

Table 2 summarizes the properties of the COd and CO2d samples, as well as the discharge properties, that is,
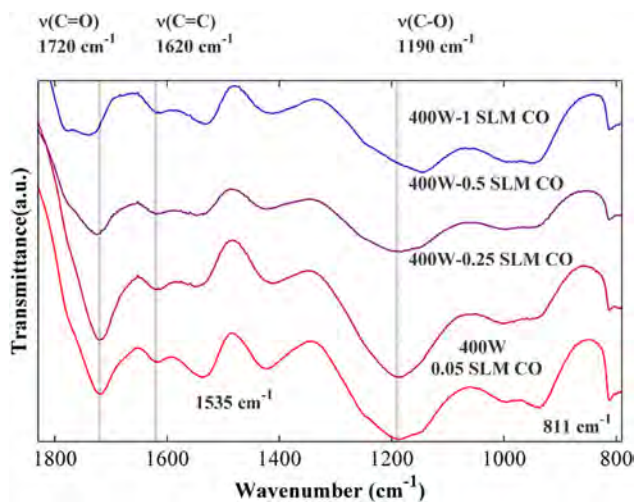

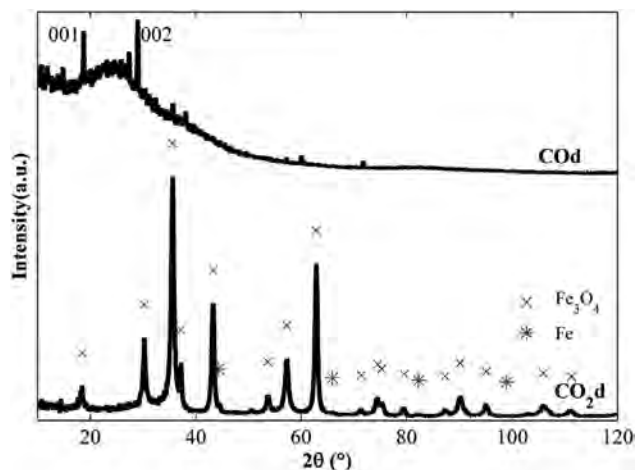**Figure 10.** FTIR spectra of the COd sample, formed at 400 W and various gas flow rates.

Figure 12. XRD spectra of the COd and CO2d samples, formed at 6000 W and 1 LM (9.1 eV/molecule).

emission characteristics and gas composition in the CO and CO_2 plasma, at 600 W input power, and 1 SLM gas flow rate. In the next section, we will try to link both, with the aim to explain the underlying mechanisms of the synthesis of both types of materials.

4. Discussion

4.1. CO Discharge and COd Sample

The CO DBD exhibits a very pronounced growth of solid deposits, in contrast to the CO_2 discharge. CO polymerization in a pressure-induced process is considered to be governed by the disproportionation reaction (Reaction 3 in the Introduction).[83,84] The same rationale can also be used for the CO discharge in the present study: (i) the activation energy of Reaction 3 is significantly lower than the C—O bond energy (5.5 eV vs. 11 eV, respectively); (ii) no O_2 was found in the exhaust, which would have been the case if there would be significant CO dissociation in the plasma; (iii) the FTIR spectrum of the COd sample is very similar to that of p-CO as obtained by Lipp;[83,84] (iv) the polymeric and mostly amorphous nature of the COd sample is confirmed in our study by different characterization techniques, including FTIR, XRD, and Raman Spectroscopy. The CO disproportionation reaction might be followed by the Reactions 14–16, accompanied by the formation of C_2O radicals and the further long polymer network growth.

To gain a better understanding of the ongoing processes, we reflect on the effect of specific energy input (SEI) variation on the properties of the discharge and the formed material. First, the larger amount of CO_2 produced in the CO plasma at higher SEI reflects the growing importance of the disproportionation reaction (Reaction 3). Second, the drop of the C_2 Swan emission

band relative intensity upon lower flow rate, and thus, higher SEI (cf. Figure 5) might indicate that less C_2 radicals are formed. Third, the SEM images and FTIR spectra (cf. Figures 6, 7, and 10) demonstrate only a slight modification of the chemical structure and morphology upon increasing SEI, and thus, no significant degradation of the polymer structure. Thus, the higher energy input might be used to maximize the deposit formation in CO discharges without complete graphitization of the solid products (judging upon the FTIR measurements presented on Figure 10). This observation is supported by the fact that the solid products obtained in the work of Geiger and Staack, synthesized with a CO plasma at 40–60 times lower power input (10 W vs. 400–600 W at similar gas flow rates) resulted in rather similar FTIR spectra. Interestingly, the reported growth rates and the formed CO_2 concentrations were one-two orders of magnitude lower as well (cf. Table 3). Some difference in elemental composition of the solid deposits can be noticed in Table 4, which might be attributed to the high sensitivity of the p-CO to atmospheric exposure, giving rise to some chemical structure modification over time.[88] Besides, different measurement techniques were applied, and hydrogen cannot be measured with XPS, which was used in our study.

Mori demonstrated that oxygen or hydrogen admixtures (0.1–1%) to a CO discharge result in solid deposits with a strongly different morphology and crystallinity, and can even suppress the formation of the deposits.[53–55,57] In our work, it was shown that a higher energy input results in a higher concentration of CO_2 in the reactor outlet gas (up to 6.2%, cf. Table 1), which may also act as amorphous phase etchant.[89] This might limit the production rate and explain the slight distortion in the structure morphology resulting from a higher SEI (cf. Figures 6 and 7). However, a detailed

Table 2. Summary of the properties of the COd and CO2d samples obtained in the CO and CO_2 DBD plasmas, respectively, as well as the optical emission characteristics and gas composition in both plasmas, measured with GC, at 600 W input power, and 1 SLM gas flow rate, corresponding to a SEI of 9.1 eV/molecule.

Material characterization	COd	CO2d
Production rate [mg/min]	ca. 15	ca. 0.15
EDX, atomic conc.%	C/O 73%/27%	Fe/O/C 13%/50%/30%
XPS, atomic conc.%	C/O	Fe/O/C/
	63%/37%	16%/60%/15%
FTIR	C=C,C=O,C—O	Fe—O, C=C, C—O
XRD	Amorphous phase, 001,002	Fe_3O_4, Fe
Raman	$I_D/I_G \sim 0.3$	Fe_3O_4, G-,D-bands
Discharge properties	**CO**	**CO_2**
OES	C_2(Swan), CO(A), CO(3B), CO_2(Fox)	CO(A), CO_2(Fox), CO(3B), Fe lines
GC	CO(98.8%), CO_2(1.2%)	CO_2(79.8%), CO(13.8%), O_2(6.4%)

Table 3. Difference between the solid materials deposited in our CO DBD, and the materials produced in the CO DBD by Geiger and Staack.[59]

Parameter	This work	Ref.[59]
Input power [W]	600	10
CO flow rate [SLM]	1	0.1–1
SEI [eV/molec.]	9.1	1.5–0.1
CO_2 produced [mol.%]	1.2%	<0.1%
Growth rate [mg min^{-1}]	ca. 15	0.16–0.20
Elemental composition, atomic conc.%	C/O	C/H/O
	63%/37% (XPS)	36%/31%/33% (pyrolysis)

study of the effect of energy input on crystallinity or C:O ratio is beyond the scope of this paper, and might be studied along with the influence of admixtures on the atmospheric pressure CO DBD and its solid products. It is also interesting to note the similarity of the achieved in the CO DBD structure to a C_3O_2 polymer, known have various applications in the chemical industry.[90]

4.2. CO_2 Discharge and CO2d Sample

As noted before, the deposition of solid products in the CO_2 DBD is limited and very few analyses are available in literature. The suppression of the formation of solid carbon structures might be explained in different ways: (i) Reactions 11–13 in the oxygen rich plasma efficiently quench C and C_2O, which are precursors for the formation of solid carbon C_s and polymerized CO; (ii) the excited CO_2 molecules and their dissociation products can actively gasify, and thus, etch the deposited carbon according to Reaction 13. The latter property of CO_2 plasmas was demonstrated for catalyst de-coking,[76] and carbon nanotube purification and functionalization.[89,91] In contrast to the CO discharge, the CO_2 plasma yields a two orders of magnitude lower deposition rate, indicating indeed that the occurring processes are different.

It is interesting to note that in our study the deposited coating of the CO_2 discharge contains both carbonaceous and inorganic compounds. The latter (together with the presence of the Fe lines in the optical emission spectrum, cf. Figure 4[a]) gives direct evidence for the fact that etching takes place on the metal electrode surface, producing nanopowders. Gushin also demonstrated the formation of nanopowders of various materials in an atmospheric pressure CO_2 plasma, albeit for a microwave (MW) plasma torch[92]. The formation of a product somewhat similar to the CO2d sample was obtained when an iron electrode was used. However, in contrast to our study, no carbon content was found. Moreover, the crystalline phases were determined to be Fe_2O_3 and FeO, while Fe_3O_4 and Fe were detected in our case. Table 4 summarizes the different plasma conditions and sample characteristics for our study, compared to the work of Gushin,[92] as well as compared to the work of Borra et al.,[93] where also nanopowders (or nanoparticles) were produced, albeit for a N_2 DBD.

The production of nanoparticles due to etching of the electrode is a known property of non-thermal plasmas.[93–95] Interestingly, the characteristic size of the metallic NPs, produced in a N_2 DBD is somewhat smaller (1...10 nm)[93] than of the NPs obtained in our study (see Table 4). It is known that the size of the produced NPs is

Table 4. Comparison between the production of the CO2d sample in this work, and the reported NP production by Gushin[92] and Borra et al.[93]

Parameter	This work	Gushin[92]	Borra et al.[93]
Type of plasma	DBD	MW	DBD
Input power [W]	600	400	1–10
Flow rate [SLM]	1, CO_2	5, CO_2	1–10, N_2
SEI [eV/molec.]	9.1	1.2	0.02..0.15
CO_2 conversion [%]	19.2	ca. 5	–
Production rate [mg min^{-1}]	0.15 (Collected powder)	0.025 (Measured electrode erosion)	$10–300 \times 10^{-6}$
Elemental composition, atomic conc.%	Fe/O/C 13%/50%/30% (EDS)	Fe/O 57%/43% (EDS)	Metallic NPs
Crystalline phases	Fe_3O_4, Fe	Fe_2O_3, FeO	–
Particle size [nm]	10..300	50..60	1..10

controlled by the energy delivered to the electrode surface via a single MD.[93,94] Thus, the increase in particle size might be explained by the higher energy of the MDs occurring in oxygen-containing atmospheres.[60,96,97] In the work of Borra et al.,[93] the energy per filament was calculated to be 10–100 µJ for 50 mA current pulses in N_2 atmosphere. We can roughly estimate that the energy per MD would be 200–500 µJ for the 100–1000 mA current pulses in our CO_2 discharge. This also explains why the input power variation has no or limited effect on the CO2d sample properties: an increase of the applied voltage (and thus input power) results in a larger number of micro-discharges, rather than in modification of their properties. Thus, a higher input power essentially increases the production rate of the solid product.

4.3. Can We Produce Carbon Materials by Means of Atmospheric Pressure CO₂ Plasma?

The aim of this paper was to answer the question whether CO and CO_2 discharges give rise to similar deposits at similar conditions (cf. the Introduction). It is clear from the above that the answer is no. At high specific energy input (SEI), e.g., 120 eV/molecule, the CO discharge yields about 6.2 mol.% CO_2 in the reactor exhaust. In spite of this limited CO_2 production, these conditions are accompanied by a significant drop of the C_2 Swan intensity (cf. Figure 5) and a modification of the chemical structure (cf. Figure 10) of the polymeric solid product. At similar SEI values, the CO_2 DBD outlet contains 56% CO_2, 30% CO, and 14% O_2 (see Figure 3). The CO_2 and O_2 molecules are known to be not only etchant agents in plasma,[89,91,98,99] but they can also quench the C_2O and C radicals (cf. Reactions 11–13) which are responsible for the formation of the carbon structure. This fact might be correlated with the absence of C_2 Swan bands in the optical emission spectrum of the CO_2 plasma. In general, this explains why the CO_2 discharge yields a much lower solid product formation, and with a different chemical structure than in the CO plasma, in spite of the fact that still a considerable amount of CO is formed.

Thus, it seems that in order to utilize the transformation $CO_2 \rightarrow CO \rightarrow C_s$ in a DBD, we have to extract the oxygen during the conversion process. For instance, the use of oxygen deficient ferrites in thermo-catalytic reactions allows the reduction of CO_2 to carbon.[100,101] In this process the oxygen produced from CO_2 gets incorporated into the surface of the active ferrite. However, it was reported that excessive amounts of CO_2 might prevent carbon formation.[102] A similar concept of oxygen extraction was reported already by Mori et al. for a CO_2 plasma, providing an interesting route to produce carbon structures in a CO_2

plasma, via the in situ extraction of the oxygen.[22] This paper confirms the fact that oxygen is one of the inhibitors of carbon deposition in a CO_2 plasma. In addition, the formation of carbon deposits is often observed in plasma systems operating in CO_2—CH_4 mixtures.[19,24,103,104] The lower amount of carbonaceous product gasification (and thus etching) via oxygen species in a CO_2—CH_4 atmosphere might be explained by trapping of the formed O_2 by the CH_x radicals, as demonstrated by Aerts et al.[105] A similar effect can be expected by admixing H_2 in CO_2 discharges, as was also reported by Aerts et al.[105]

5. Conclusion

The question to be answered by this paper was whether CO and CO_2 discharges give rise to similar deposits at similar conditions (see Introduction). To answer this question, we have analyzed and compared CO and CO_2 DBD plasmas, and their solid products. It is clear that substantial differences in the plasma composition result in the formation of deposits that are remarkably different. The CO DBD yields a two orders of magnitude higher deposition rate than the CO_2 discharge, indicating that the underlying processes are indeed different. The deposition in the CO plasma seems to be driven by the disproportionation reaction (i.e., $CO + CO \rightarrow C + CO_2$), as a significant amount of CO_2 (up to 6.2 mol.%), proportional to the specific energy input, was found in the reactor exhaust. The solid product is characterized as an amorphous carbonaceous (C/O=63%/37%) structure and identified as polymeric CO. The p-CO structure might potentially be close C_3O_2 polymer, valuable chemical product. The CO_2 discharge, on the other hand, does not produce this carbonaceous structure, in spite of the fact that considerable amounts of CO are produced. Indeed, the outlet mixture of the CO_2 discharge contains besides CO_2 also CO and O_2. The Fe lines present in the OES spectrum, however, indicate that significant oxidation and etching takes place on the surface of the metal electrode, which results in the formation of nanoparticles (Fe/O/C=16%/60%/15%, Fe_3O_4) in the microdischarges and as deposits on the reactor walls. At the same time, the formation of the amorphous carbonaceous structure close to polymeric CO is suppressed, due to etching by the CO_2 and O_2 molecules, and because the latter also quench the C and C_2O radicals, which are the precursors for this carbonaceous structure. Thus, we believe that in order to produce such a carbonaceous structure from a DBD in CO_2 (i.e., through the transformation $CO_2 \rightarrow CO \rightarrow C_s$), the O_2 produced by CO_2 splitting should be extracted during the conversion process.

[1] G. Centi S. Perathoner, Catalysis Today Special Issue of the 10th Int. Conf. on CO_2 Utilization, Tianijn, China **2009** *148*, 191.

[2] S. Ahmed, A. Aitani, F. Rahman, A. Al-Dawood, F. Al-Muhaish, *App. Catal. A: Gen*. **2009**, *359*, 1.

[3] G. S. Simate, S. E. Iyuke, S. Ndlovu, C. S. Yah, L. F. Walubita, *J. Nat. Gas Chem*. **2010**, *19*, 453.

[4] S. Rodat, S. Abanades, G. Flamant, *J. Sol. Energy Eng*. **2011**, *133*, 031001.

[5] K. Michiels, B. Peeraer, W. Van Dun, J. Spooren, V. Meynen, Faraday Discussions **2015** *183*, 177.

[6] S. Bajracharya, A. ter Heijne, X. Dominguez Benetton, K. Vanbroekhoven, C. J. N. Buisman, D. P. B. T. Strik, D. Pant, *Microb. Fuel Cells* **2015**, *195*, 14.

[7] J. Ren, F. F. Li, J. Lau, L. Gonzaílez-Urbina, S. Licht, *Nano Lett*. **2015**, *15*, 6142.

[8] A. Fridman, *Plasma Chemistry*. Cambridge University Press, New York **2008**.

[9] A. Bogaerts, T. Kozak, K. van Laer, R. Snoeckx, Faraday Discussions **2015** *183*, 217.

[10] F. Fabry, G. Flamant, L. Fulcheri, *Chem. Eng. Sci*. **2001**, *56*, 2123.

[11] L. Fulcheri, N. Probst, G. Flamant, F. Fabry, E. Grivei, X. Bourrat, *Third International Conference on Carbon Black* **2002**, *40*, 169.

[12] J. R. Fincke, R. P. Anderson, T. A. Hyde, B. A. Detering, *Ind. Eng. Chem. Res*. **2002**, *41*, 1425.

[13] A. Kobayashi, K. Osaki, C. Yamabe, 3rd International Symposium on Applied Plasma Science (ISAPS 01) **2002**, *65*, 475.

[14] W. Cho, S. H. Lee, W. S. Ju, Y. Baek, J. K. Lee, *Catal. Today* **2004**, *98*, 633.

[15] M. P. Srivastava, A. Kobayashi, *Trans. JWRI* **2010**, *39*, 11.

[16] R. Pristavita, N. Y. Mendoza-Gonzalez, J. L. Meunier, D. Berk, *Plasma Chem. Plasma Process*. **2010**, *30*, 267.

[17] S. Kim, M. Lim, Y. Chun, *Plasma Chem. Plasma Process*. **2014**, *34*, 125.

[18] H. J. Gallon, X. Tu, M. V. Twigg, J. C. Whitehead, *App. Catal. B: Environ*. **2011**, *106*, 616.

[19] X. Tu, J. C. Whitehead, *Int. J. Hydrogen Energ*. **2014**, *39*, 9658.

[20] S. Mahammadunnisa, E. L. Reddy, D. Ray, C. Subrahmanyam, J. C. Whitehead, *Int. J. Greenh. Gas Con*. **2013**, *16*, 361.

[21] G. Hirson, G. F. Shouse, M. W. Shuey, Systems and methods of plasma partial dissociation of carbon dioxide, water, and carbonaceous matter, WO 2015089069 A1, **2015**.

[22] S. Mori, N. Matsuura, L. L. Tun, M. Suzuki, *Plasma Chem. Plasma Process*. **2015**, *36*, 231.

[23] G. Petitpas, J. D. Rollier, A. Darmon, J. Gonzalez-Aguilar, R. Metkemeijer, L. Fulcheri, *Int Conf on Materials for Hydrogen Energy: Solar Hydrogen (ICMHE 2004)* **2007**, *32*, 2848.

[24] M. Li, G. Xu, Y. Tian, L. Chen, H. Fu, *J. Phys. Chem. A*. **2004**, *108*, 1687.

[25] S. L. Suib, S. L. Brock, M. Marquez, J. Luo, H. Matsumoto, Y. Hayashi, *J. Phys. Chem. B*. **1998**, *102*, 9661.

[26] S. L. Brock, M. Marquez, S. L. Suib, Y. Hayashi, H. Matsumoto, *J. Catal*. **1998**, *180*, 225.

[27] J. Y. Wang, G. G. Xia, A. Huang, S. L. Suib, Y. Hayashi, H. Matsumoto, *J. Catal*. **1999**, *185*, 152.

[28] H. Matsumoto, S. Tanabe, K. Okitsu, Y. Hayashi, S. L. Suib, *Bull. Chem. Soc. Jpn*. **1999**, *72*, 2567.

[29] G. Zheng, J. Jiang, Y. Wu, R. Zhang, H. Hou, *Plasma Chem. Plasma Process*. **2003**, *23*, 59.

[30] R. Li, Y. Yamaguchi, S. Yin, Q. Tang, T. Sato, *Proc. 15 Int. Symp. Reactiv. Solids* **2004**, *172*, 235.

[31] R. Li, Q. Tang, S. Yin, T. Sato, *Fuel Process. Technol*. **2006**, *87*, 617.

[32] R. Li, Q. Tang, S. Yin, T. Sato, *App. Phys. Lett*. **2007**, *90*, 131502.

[33] S. Paulussen, B. Verheyde, X. Tu, C. De Bie, T. Marterns, D. Petrovic, A. Boagaerts, B. Sels, *Plasma Sources Sci. Technol*. **2010**, *19*, 034015.

[34] M. A. Lindon, E. Scime, *Front. Phys*. **2014**, *2*, 1.

[35] M. Ramakers, I. Michielsen, R. Aerts, V. Meynen, A. Bogaerts, *Plasma. Process. Polym*. **2015**, *12*, 755.

[36] R. Aerts, W. Somers, A. Bogaerts, *Chem. Sus. Chem* **2015**, *8*, 702.

[37] F. Brehmer, S. Welzel, M. C. M. van de Sanden, R. Engeln, *J. Appl. Phys*. **2015**, *116*, 123303.

[38] D. Mei, Y. L. He, S. Liu, J. Yan, X. Tu, *Plasma Process. Polym*. **2015**, *13*, 544.

[39] A. Ozkan, T. Dufour, T. Silva, N. Britun, R. Snyders, A. Bogaerts, F. Reniers, *Plasma Sources Sci. Technol*. **2016**, *25*, 025013.

[40] D. Mei, X. Zhu, Y.-L. He, J. D. Yan, X. Tu, *Plasma Sources Sci. Technol*. **2015**, *24*, 015011.

[41] T. Tomai, T. Ito, K. Terashima, *The Joint Meeting of 7th APCPST (Asia Pacific Conference on Plasma Science and Technology) and 17th SPSM (Symposium on Plasma Science for Materials)* **2006**, *506–507*, 409.

[42] T. Tomai, K. Katahira, H. Kubo, Y. Shimizu, T. Sasaki, N. Koshizaki, K. Terashima, *J. Supercritical Fluids* **2007**, *41*, 404.

[43] K. Van Laer, A. Boagaerts, *Energy. Technol*. **2015**, *3*, 1038.

[44] K. Jogan, A. Mizuno, T. Yamamoto, J. Chang, *IEEE Trans. Ind. App*. **1993**, *29*, 876.

[45] D. Yap, J. M. Tatibouet, C. Batiot-Dupeyrat, *J. CO_2 Util*. **2015**, *12*, 54.

[46] P. Nikolaev, M. J. Bronikowski, R. K. Bradley, F. Rohmund, D. T. Colbert, K. A. Smith, R. E. Smalley, *Chem. Phys. Lett*. **1999**, *313*, 91.

[47] P. Nikolaev, *J. Nanosci. Nanotechnol*. **2004**, *4*, 307.

[48] A. G. Nasibulin, A. S. Anisimov, P. V. Pikhitsa, H. Jiang, D. P. Brown, M. Choi, E. I. Kauppinen, *Chem. Phys. Lett*. **2007**, *446*, 109.

[49] A. S. Anisimov, A. G. Nasibulin, H. Jiang, P. Launois, J. Cambedouzou, S. D. Shandakov, E. I. Kauppinen, *Carbon* **2010**, *48*, 380.

[50] E. Plönjes, P. Palm, G. Babu Viswanathan, V. V. Subramaniam, I. V. Adamovich, W. R. Lempert, H. L. Fraser, J. William Rich, *Chem. Phys. Lett*. **2002**, *352*, 342.

[51] Y. Su, Z. Yang, H. Wei, E.S. -W. Kong, Y. Zhang, *Appl. Surf. Sci*. **2011**, *257*, 3123.

[52] Z. Bo, Y. Yang, J. Chen, K. Yu, J. Yan, K. Cen, *Nanoscale* **2013**, *5*, 5180.

[53] S. Mori, M. Suzuki, *Diam. Relat. Mater.* **2008**, *17*, 999.

[54] S. Mori, M. Suzuki, *J. Chem. Eng. Jpn.* **2009**, *42*, S249.

[55] S. Mori, M. Suzuki, *Diam. Relat. Mater.* **2009**, *18*, 678.

[56] S. Mori. M. Suzuki, *The proceedings of the 1st International Conference on Microelectronics and Plasma Technology (ICMAP 2008)* **2009**, *517*, 4264.

[57] Y. Anekawa, S. Mori, M. Suzuki, *The 21st International Symposium on Plasma Chemistry (ISPC-21)* **2013**.

[58] A. D. C. Permana, A. Kameyama, M. Suzuki, S. Mori, *The 22nd International Symposium on Plasma Chemistry (ISPC-22)*.

[59] R. Geiger, D. Staack, *J. Phys. D: Appl. Phys.* **2011**, *44*, 274005.

[60] I. Belov, S. Paulussen, A. Boagaerts, *Plasma Sources Sci. Technol.* **2016**, *25*, 015023.

[61] R. Snoeckx, Y. X. Zeng, X. Tu, A. Bogaerts, *RSC Adv.* **2015**, *5*, 29799.

[62] V. G. Samoilovich, V. I. Gibalov, K. V. Kozlov, *Physical Chemistry of the Barrier Discharge*, 2nd edition, Deutscher Verlag für Schweisstechnik, Düsseldorf **1997**.

[63] P. Bruggeman, R. Brandenburg, *J. Phys. D: Appl. Phys.* **2013**, *46*, 464001.

[64] R. Aerts, T. Martens, A. Bogaerts, *J. Phys. Chem. C* **2012**, *116*, 23257.

[65] C. Gorse, M. Cacciatore, M. Capitelli, *Chem. Phys.* **1984**, *85*, 165.

[66] A. Vesel, M. Mozetic, A. Drenik, M. Balat-Pichelin, *Chem. Phys.* **2011**, *382*, 127.

[67] A. Vesel, R. Zaplotnik, J. Iacono, M. Balat-Pichelin, M. Mozetic, *Sensors* **2012**, *12*, 16168.

[68] Z. Machala, M. Janda, K. Hensel, I. Jedlovský, L. Leštinská, V. Foltin, V. Martišovitš, M. Morvová, *J. Mol. Spectrosc.* **2007**, *243*, 194.

[69] G. W. Fox, O. S. Duffendack, E. F. Barker, *Proc. Natl. Acad. Sci. USA* **1927**, *13*, 302.

[70] T. Silva, N. Britun, T. Godfroid, R. Snyders, *Plasma Sources Sci. Technol.* **2014**, *23*, 025009.

[71] F. Brehmer, *PhD Thesis Thesis*, Technical University of Eindhoven, **2015**.

[72] T. Oh, *MSc Thesis Thesis*, University of Illinois at Urbana-Champaign, **2013**.

[73] L. F. Spencer, A. D. Gallimore, *Plasma Sources Sci. Technol.* **2013**, *22*, 015019.

[74] Y. Babou, P. Rivière, M. Y. Perrin, A. Soufiani, *Plasma Sources Sci. Technol.* **2008**, *17*, 045010.

[75] D. L. Quang, Y. Babou, P. Andre, *IOP Conference Series: Materials Science and Engineering* **2012**, *29*, 012009.

[76] S. Kameshima, K. Tamura, Y. Ishibashi, T. Nozaki, *Catal. Today* **2015**, *256*, 67.

[77] P. Caubet, G. Dorthe, *Chem. Phys. Lett.* **1994**, *218*, 529.

[78] N. Krstulovic, U. Cvelbar, A. Vesel, S. Milosevic, M. Mozetic, *Mater. Technol.* **2009**, *43*, 245.

[79] M. Mozetic, U. Cvelbar, A. Vesel, N. Krstulovic, S. Milosevic, *IEEE Transac. Plasma Sci.* **2008**, *36*, 868.

[80] D. Kozak, E. Shibata, A. Iizuka, T. Nakamura, *Carbon* **2014**, *70*, 87.

[81] M. P. Danilaev, E. A. Bogoslov, O. G. Morozov, A. R. Nasybullin, D. M. Pashin, Y. E. Pol'skii, *J. Eng. Phys. Thermophys.* **2015**, *88*, 774.

[82] C. Cunha, S. Panseri, D. Iannazzo, A. Piperno, A. Pistone, M. Fazio, A. Russo, M. Marcacci, S. Galvagno, *Nanotechnology* **2012**, *23*, 465102.

[83] M. J. Lipp, W. J. Evans, B. J. Baer, C. S. Yoo, *Nat. Mater.* **2005**, *4*, 211.

[84] W. J. Evans, M. J. Lipp, C. S. Yoo, H. Cynn, J. L. Herberg, R. S. Maxwell, M. F. Nicol, *Chem. Mater.* **2006**, *18*, 2520.

[85] P. K. Chu, L. Li, *Mater. Chem. Phys.* **2006**, *96*, 253.

[86] S. Prawer, R. J. Nemanich, *Phil. Trans. R. Soc. Lond. A: Math. Phys. Eng. Sci.* **2004**, *362*, 2537.

[87] Y.-S. Li, J. S. Church, A. L. Woodhead, *J. Magn. Magn. Mater.* **2012**, *324*, 1543.

[88] M. Ceppatelli, A. Serdyukov, R. Bini, H. J. Jodl, *J. Phys. Chem. B.* **2009**, *113*, 6652.

[89] D. J. Babu, S. Yadav, T. Heinlein, G. Cherkashinin, J. Â. J. Schneider, *J. Phys. Chem. C.* **2014**, *118*, 12028.

[90] A. Fridman, A. F. Gutsol, Y. I. Cho, Production and uses of carbon suboxides, US 7,569,203 B2, **2009**.

[91] F. Pourfayaz, Y. Mortazavi, A. A. Khodadadi, S.-H. Jafari, *Appl. Phys. A* **2012**, *106*, 829.

[92] P. Gushin, *PhD-thesis Thesis*, Gubkin Russian State Oil and Gas University, Moscow, **2008**.

[93] J. P. Borra, N. Jidenko, J. Hou, A. Weber, *J. Aerosol Sci.* **2015**, *79*, 109.

[94] T. V. Pfeiffer, J. Feng, A. Schmidt-Ott, *Adv. Powder Technol.* **2014**, *25*, 56.

[95] L. Lin, Q. Wang, *Plasma Chem. Plasma Process.* **2015**, *35*, 925.

[96] H. Höft, M. Kettlitz, K. D. Weltmann, R. Brandenburg, *J. Phys. D: Appl. Phys.* **2014**, *47*, 455202.

[97] P. Audier, H. Rabat, A. Leroy, D. Hong, *Plasma Sources Sci. Technol.* **2014**, *23*, 065045.

[98] A. Drenik, L. Salamon, R. Zaplotnik, A. Vesel, M. Mozetič, *Vacuum* **2013**, *98*, 45.

[99] A. Vesel, K. Eleršič, M. Modic, I. Junkar, M. Mozetič, *Materials* **2014**, *7*, 2014.

[100] Y. Tamaura, M. Tahata, *Nature* **1990**, *346*, 255.

[101] T. Kodama, T. Sano, T. Yoshida, M. Tsuji, Y. Tamaura, *Carbon* **1995**, *33*, 1443.

[102] K. Ehrensberger, R. Palumbo, C. Larson, A. Steinfeld, *Ind. Eng. Chem. Res.* **1997**, *36*, 645.

[103] A. Ozkan, T. Dufour, G. Arnoult, P. De Keyzer, A. Bogaerts, F. Reniers, *J. CO2 Util.* **2015**, *9*, 74.

[104] T. Xin, J. G. Hellen, V. T. Martyn, A. G. Peter, J. C. Whitehead, *J. Phys. D: Appl. Phys.* **2011**, *44*, 274007.

[105] R. Aerts, R. Snoeckx, A. Bogaerts, *Plasma Process. Polym.* **2014**, *11*, 985.